INTERNATIONAL JOURNAL FOR NUMERICAL METHODS IN FLUIDS, VOL. 16, 105–131 (1993)

NUMERICAL PROBLEMS IN SIMULATING TIDAL FLOWS WITH A FRICTIONAL-VELOCITY-DEPENDENT EDDY VISCOSITY AND THE INFLUENCE OF STRATIFICATION

ALAN M. DAVIES

Proudman Oceanographic Laboratory, Bidston Observatory, Birkenhead, Merseyside L43 7RA, U.K.

SUMMARY

The paper deals with the accurate determination of tidal current profiles in both homogeneous and stratified regions when a no-slip condition is used at the seabed with a flow-dependent eddy viscosity related to the depth-mean current or the bed frictional velocity.

Calculations show that it is essential to accurately resolve the high-shear region which occurs at the bed and across the pycnocline/thermocline in the case of stratified flow. A computationally accurate and economic method of resolving these regions is demonstrated using the Galerkin method with a set of basis functions designed to accurately reproduce the high-shear layers which occur in these regions.

With a flow-independent eddy viscosity a stability analysis can be readily performed and an unconditionally stable algorithm developed. However, with a flow-dependent viscosity, in particular a viscosity computed from the frictional velocity, a non-linear numerical instability can occur. A method of maintaining numerical stability in this case is also described.

The importance of near-bed resolution to the computed value of the frictional velocity is demonstrated and its influence on the total tidal velocity profile is illustrated by a number of idealized calculations using various eddy viscosity formulations.

The influence of stratification on the computed tidal profiles is shown in the latter part of the paper.

KEY WORDS Tidal-currents Stratification Galerkin Spectral Log-layer Resolution B-spline

1. INTRODUCTION

Although a significant number of three-dimensional models based upon a slip condition at the seabed exist in the literature,[1–8] very little has been done with no-slip bottom boundary resolution models[9] even though this region is important for a number of physical processes (e.g. sediment transport).

The solution of the hydrodynamic equations using a mixed finite difference/spectral approach[10] is now well formulated. Recently the method has been extended in the case of a wind-driven flow problem to the use of a mixed basis set[11–13] in which an additional function is used to take into account the high-shear surface-wind-driven layer, giving a faster rate of convergence of the series.[11] A similar approach has been used at the seabed[14] with a slip condition.

In this paper we consider the application of a mixed basis set to the problem of tidal flow with a no-slip bottom boundary condition. The basis set is composed of a set of eigenfunctions (modes) computed from the eddy viscosity profile and an additional function with a logarithmic profile in the near-bed region. By computing the eigenfunctions using an expansion of B-splines with a knot

0271–2091/93/020105–27$18.50

Received March 1992
Revised July 1992

spacing in the near-bed region based on a logarithmic or log–linear distribution, a set of modes with a high-shear near-bed profile can be determined. In this case a faster rate of convergence and a more accurate solution are determined using only the modal expansion. Initially the eddy viscosity is taken as constant in time. Subsequently a number of flow-dependent time-varying eddy viscosity formulations are used, namely viscosity proportional to water depth and depth-mean current.[15,17] A physically interesting formulation is also considered (which has not previously been examined with the Galerkin/spectral method), namely one in which the viscosity is related to a time varying bed frictional velocity. Such a formulation gives rise to highly non-linear terms which can cause numerical instabilities.[18] A method of overcoming these instabilities is presented in the paper. Calculations clearly show that in the case of a frictional-velocity-dependent eddy viscosity it is essential to ensure that the expansion functions can adequately resolve the high-shear near-bed gradients. Such a requirement is not so critical for the other forms of eddy viscosity.

In the latter part of the paper the problem of generating an accurate set of modes and resolving the high-shear near-bed layer and also the shear layer within the pycnocline which occurs in stratified flows is considered.

The importance of the turbulence intensity below, within and above the pycnocline in determining the tidal current profile is considered.

The modal method developed here is a computationally economic means of resolving the high-shear layer across the thermocline and at the seabed. The implications for finite difference methods or the Galerkin method with discontinuous functions (the finite element method) are discussed in the latter part of the paper in terms of resolution problems encountered with the spectral/modal method when poor resolution is used to compute the modes.

Although the method is developed in this paper in terms of a single-point model in the vertical, it can be readily extended to a full three-dimensional model.[3,6,19]

2. POINT MODEL AND NUMERICAL SOLUTION

2.1. Point model in the vertical

For a single-point model in the vertical the linear hydrodynamic equations are

$$\frac{\partial u}{\partial t}-\gamma v=\frac{\partial P}{\partial x}+\frac{1}{h^2}\frac{\partial}{\partial \sigma}\left(\mu\frac{\partial u}{\partial \sigma}\right), \tag{1}$$

$$\frac{\partial v}{\partial t}+\gamma u=\frac{\partial P}{\partial y}+\frac{1}{h^2}\frac{\partial}{\partial \sigma}\left(\mu\frac{\partial v}{\partial \sigma}\right), \tag{2}$$

with $\sigma=z/h$ a vertically normalized sigma co-ordinate. In these equations t is time, x, y and z are Cartesian co-ordinates and u and v are the x- and y-components of velocity respectively. The geostrophic coefficient γ is taken as constant, with μ the vertical eddy viscosity and h the water depth.

In the point model flow is forced by oscillatory pressure gradients $\partial P/\partial x$ and $\partial P/\partial y$; we express $\partial P/\partial x$ and $\partial P/\partial y$ as

$$\partial P/\partial x=h_x\omega\cos(\omega t), \tag{3}$$

$$\partial P/\partial y=h_y\omega\cos(\omega t), \tag{4}$$

with h_x and h_y the amplitude components of the oscillatory forcing of frequency ω.

For tidal flow a zero-stress surface boundary condition is applied, namely

$$-\rho\left(\frac{\mu}{h}\frac{\partial u}{\partial \sigma}\right)_0=0, \qquad -\rho\left(\frac{\mu}{h}\frac{\partial v}{\partial \sigma}\right)_0=0, \tag{5}$$

with ρ the density of sea-water.

At the seabed a no-slip condition is used, i.e.

$$u=v=0. \tag{6}$$

2.2. Numerical solution in the vertical

Only the major steps in solving the hydrodynamic equations using the Galerkin method with a mixed basis set will be described, since a more detailed development can be found in References 10, 11, 14 and 18.

We express the u- and v-components of velocity as

$$u=\psi_u+\sum_{r=1}^{m} A_r f_r(\sigma), \qquad v=\psi_v+\sum_{r=1}^{m} B_r f_r(\sigma), \tag{7a}$$

where $\psi_u(x, y, \sigma, t)$ and $\psi_v(x, y, \sigma, t)$ are specified external functions sastisfying the essential boundary condition (6) and coefficients $A_r(x, y, t)$ and $B_r(x, y, t)$ are expansion coefficients in the vertical, to be determined using the Galerkin approach, with $f_r(\sigma)$ the m basis functions.

Obviously, once the coefficients A_r and B_r in expansions (7a) have been obtained, the current at any depth can be computed and its value for a range of expansion lengths M can be used to examine the rate of convergence of the expansion.

Another indicator of the accuracy of the solution, which as we will show is particularly important when a bed-stress- (frictional-velocity) related eddy viscosity is used (not previously examined with the Galerkin/modal method), is the value of the two bed stress components τ_B^x and τ_B^y given by

$$\begin{aligned}
\tau_B^x &= -\rho\frac{\mu_0}{h}\left(\frac{\partial u}{\partial \sigma}\right)_0 = -\rho\frac{\mu_0}{h}\left(\psi_u'(0)+\sum_{r=1}^{m} A_r f_r'(0)\right),\\
\tau_B^y &= -\rho\frac{\mu_0}{h}\left(\frac{\partial v}{\partial \sigma}\right)_0 = -\rho\frac{\mu_0}{h}\left(\psi_v'(0)+\sum_{r=1}^{m} B_r f_r'(0)\right),
\end{aligned} \tag{7b}$$

where μ_0 is the eddy viscosity value at the seabed, with ψ_u', ψ_v' and f_r' indicating the vertical derivatives of these functions.

Consider for illustrative purposes the solution of equation (1) using the Galerkin method, *without* rotational effects. Substituting expansions (7a) in equation (1) and applying the Galerkin method whereby the resulting equation is multiplied by f_r and integrated from the sea surface to the sea-bed, we obtain

$$\sum_{r=1}^{m}\frac{\partial A_r}{\partial t}\int_0^1 f_r f_k\,\mathrm{d}\sigma=\frac{\partial P}{\partial x}\int_0^1 f_k\,\mathrm{d}\sigma-\frac{\alpha}{h^2}\sum_{r=1}^{m} A_r\int_0^1 \Phi\frac{\mathrm{d}f_r}{\mathrm{d}\sigma}\frac{\mathrm{d}f_k}{\mathrm{d}\sigma}\,\mathrm{d}\sigma+\frac{\mu}{h^2}\frac{\partial u}{\partial \sigma}\bigg|_1 f_k(1)-\frac{\mu}{h^2}\frac{\partial u}{\partial \sigma}\bigg|_0 f_k(0)+F_e,$$
$$k=1, 2, \ldots, m \tag{8}$$

where

$$F_e=-\int_0^1\frac{\partial \psi_u}{\partial t}f_r\,\mathrm{d}\sigma-\frac{\alpha}{h^2}\int_0^1\frac{\partial \psi_u}{\partial \sigma}\frac{\partial f_r}{\partial \sigma}\,\mathrm{d}\sigma. \tag{9}$$

In deriving (8), we have expressed the eddy viscosity as

$$\mu = \alpha(t)\Phi(\sigma), \tag{10}$$

with $\alpha(t)$ a time-varying coefficient and $\Phi(\sigma)$ a specified viscosity profile. Equation (8) can be further simplified by applying the essential boundary condition (6), namely

$$f_k(1) = 0 \quad \text{for all } k, \tag{11}$$

and the natural boundary condition (5), giving

$$\sum_{r=1}^{m} \frac{\partial A_r}{\partial t} \int_0^1 f_r f_k \, d\sigma = \frac{\partial P}{\partial x} \int_0^1 f_k \, d\sigma - \frac{\alpha}{h^2} \sum_{r=1}^{m} A_r \int_0^1 \Phi \frac{df_r}{d\sigma} \frac{df_k}{d\sigma} \, d\sigma + F_e. \tag{12}$$

Equation (12) is similar to that derived by Davies and Aldridge[20] (although they used a slip condition), except for the additional term F_e arising from the specified function ψ_u. A similar equation to (9) can be derived for the v-equation of motion, with the two equations coupled by rotation. A detailed description of the solution of the full three-dimensional equations using the Galerkin approach can be found in References 10, 11, 14, 19, 21 and 22.

2.3. An eigenfunction/modal basis set; a spectral approach

Although any function can be used as a basis function in the Galerkin approach, Davies[10,11,14,18,21] has shown the computational advantages of choosing the f_r to be eigenfunctions of

$$\frac{d}{d\sigma}\left(\Phi \frac{df}{d\sigma}\right) = -\varepsilon f, \tag{13}$$

with ε_r the associated eigenvalues.

With the boundary conditions (5) and (6), equation (13) is solved subject to

$$\left.\frac{df_r}{d\sigma}\right|_0 = 0, \qquad f_r(1) = 0. \tag{14}$$

Equation (12) can be further simplified by using the orthogonality property of eigenfunctions, namely

$$\int_0^1 f_r f_k \, d\sigma = 0, \quad r \neq k, \tag{15}$$

and normalizing the eigenfunctions such that they are unity at the sea surface; thus

$$f_r(0) = 1, \quad r = 1, 2, \ldots, m. \tag{16}$$

Writing for convenience expansions (7a) in the form

$$u = \psi_u + \sum_{r=1}^{m} u_r \phi_r f_r, \qquad v = \psi_v + \sum_{r=1}^{m} v_r \phi_r f_r, \tag{17}$$

where

$$A_r = u_r \phi_r \quad \text{and} \quad B_r = v_r \phi_r, \quad \text{with} \quad \phi_r = 1 \Big/ \int_0^1 f_r f_r \, d\sigma,$$

equation (12) simplifies to (at a single point with no x-, y-dependence of u_r, v_r)

$$\frac{du_r}{dt}=\frac{dP}{\partial x}a_r-\frac{\alpha}{h^2}\varepsilon_r u_r+F_e, \tag{18}$$

where

$$a_r=\int_0^1 f_r\,d\sigma.$$

2.4. Determination of eigenfunctions

The eigenvalue problem (13) is solved by computing the eigenfunctions in terms of an expansion of fourth-order B-splines (Figure 1). Details are given in Reference 10 and will not be repeated here. The fourth-order B-splines are piecewise polynomials which are non-zero only over a finite interval. Points along the σ-axis at which the B-spline changes from zero to non-zero are termed knots, denoted λ_i (Figure 1). The number and positioning of the knots are arbitrary and hence the resolution can be increased in any region. Davies[11,21] showed that with a no-slip bottom boundary condition in which the bed eddy viscosity was low (μ(bed)=0·0001 m^2 s^{-1}, a physically realistic value) the knot spacing had to be of the order of 0·000 05 of the water depth in the near-bed region. Davies[11,21] used 60 knots in the vertical with an arbitrary knot spacing in order to achieve accurate eigenfunctions. However, in the case of a no-slip bottom boundary condition with a near-bed linear increase in eddy viscosity (a physically correct variation) the eigenfunctions will have a logarithmic behaviour in the near-bed region[23] and hence a logarithmic or near-logarithmic distribution of B-splines would be advantageous.

This can be readily achieved using a logarithmic transform of the form

$$S=\ln(\tilde{z}/S_0)/\beta, \quad \text{with} \quad \beta=\ln(\tilde{z}/h), \quad \text{where} \quad \tilde{z}=1-z, \tag{19a}$$

or a log–linear transform of the form

$$S=\left[\ln\left(\frac{\tilde{z}}{S_0}\right)+\left(\frac{\tilde{z}-S_0}{S_*}\right)\right]\Big/\beta, \quad \text{with} \quad \beta=\ln\left(\frac{h}{S_0}\right)+\left(\frac{h-S_0}{S_*}\right). \tag{19b}$$

In these transformations S_0 is a small parameter determining the fineness of the knot spacing in

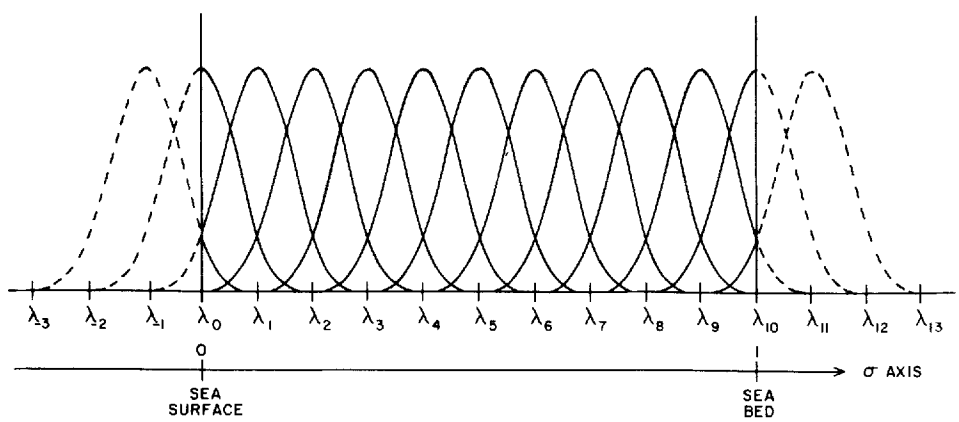

Figure 1. Distribution B-splines and associated knots with depth

the near-bed region. The parameter S_* in the log–linear transformation is an arbitrary height above the seabed over which the knot distribution is essentially logarithmic, changing to a near-linear distribution above this height. By this means an optimal distribution of B-splines in the near-bed region suitable for solving the eigenvalue problem is obtained.

2.5. *Determination of the additional functions ψ_u and ψ_v*

Just what form the additional functions ψ_u and ψ_v should take to improve the rate of convergence of the expansion is difficult to determine. Davies[11] used piecewise linear functions or trigonometric functions scaled with the wind stress to improve the convergence in the surface layer in a wind-driven flow problem. An enhanced rate of convergence in the near-bed region with a slip bottom boundary condition was obtained using similar functions scaled with the bed stress.[14] In both these cases the vertical derivative of the functions used in the expansions was zero at the sea surface and seabed, leading to a slower rate of convergence in the surface and bed boundary layers. In the present case, as we will show later, the bed stress evaluated with the modal expansion converges rapidly to the true bed stress, a situation very different from that occurring previously[11,14] where the stress computed from the expansion remained zero irrespective of the number of terms.

In the near-bed region a logarithmic behaviour of the current profile appears appropriate and hence we chose

$$\psi_u = \lambda_u \psi(z), \qquad \psi_v = \lambda_v \psi(z) \tag{20a, b}$$

with λ_u and λ_v scaling factors; $\psi(z)$ is chosen to be consistent with the logarithmic transformation (19) and is given by

$$\psi(z) = \ln(\tilde{z}/E_s)/\beta, \quad \text{with} \quad \beta = \ln(\tilde{z}/h), \quad \text{where} \quad \tilde{z} = 1 - z. \tag{21a}$$

For a pressure-driven flow the scaling factors λ_u and λ_v should be related to the external forces; thus

$$\bar{\lambda}_u = = \lambda \partial P/\partial x, \qquad \bar{\lambda}_v = \lambda \partial P/\partial y, \tag{21b}$$

with λ an arbitrary scaling factor, the magnitude of which has to be specified together with the parameter E_s in (21a). This form of scaling with external forcing is consistent with that used previously in References 11, 14 and 18, where the magnitude of the additional functions ψ_u and ψ_v were scaled with the external wind stress. The influence of variations in E_s and λ on the computed current profile will be examined in the next section.

2.6. *Profile of eddy viscosity*

Consider initially the eddy viscosity profile in homogeneous seas. On the basis of measurements in the Irish Sea[16,17] and boundary layer theory, the viscosity should increase linearly with height above the seabed up to a height h_1 of order (0·1–0·2) h. At the seabed the viscosity is given by

$$\mu_0 = K_0 U_* Z_0, \tag{22}$$

where $K_0 = 0{\cdot}4$ is Von Karman's constant, U_* is the frictional velocity of order 1–5 cm s^{-1} and Z_0 is the bed roughness of order 0·1–1 cm, giving μ_0 of order 0·05–2 cm^2 s^{-1} (0·0002 m^2 s^{-1}).

Above h_1 the eddy viscosity can be assumed constant (Figure 2, profile (A)) at a value μ_1 given by[16,17]

$$\mu_1 = K_1 h \bar{u}, \tag{23}$$

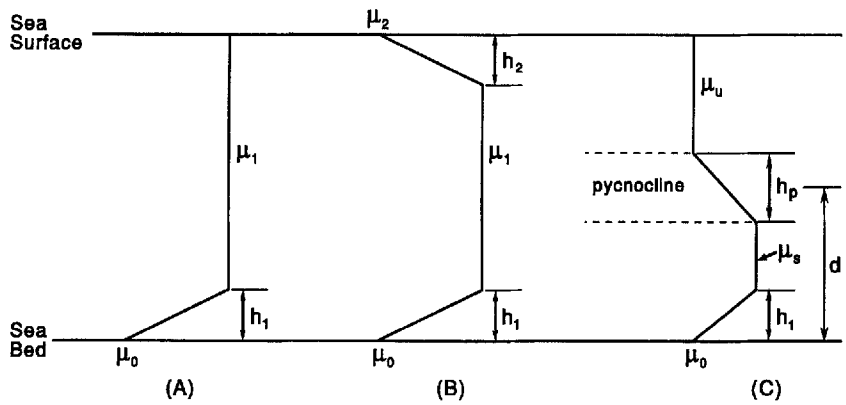

Figure 2. Schematic representation of various eddy viscosity profiles $V(\sigma)$ used in the calculations

with $\bar{u}$ the depth-mean tidal velocity and K_1 a constant of order 0·0025. Taking $\bar{u}=100\ \mathrm{cm\,s^{-1}}$, a typical tidal velocity, and $h=40$ m, a characteristic shallow-sea depth, gives $\mu_1=1000\ \mathrm{cm^2\,s^{-1}}$ ($0{\cdot}1\ \mathrm{m^2\,s^{-1}}$).

An alternative formulation[1] gives

$$\mu_1=K_2\bar{u}^2/\omega. \tag{24}$$

Taking $K_2=2\times10^{-5}$ a constant, $\omega=10^{-4}$, a typical frequency for tidal motion, and $\bar{u}=100\ \mathrm{cm\,s^{-1}}$ gives $\mu_1=2000\ \mathrm{cm^2\,s^{-1}}$ ($0{\cdot}2\ \mathrm{m^2\,s^{-1}}$). Both equations (23) and (24) suggest a $\mu_1:\mu_0$ ratio of order 1000:1.

By analogy with the seabed and from recent results obtained with turbulence energy models,[9,22] a decrease in viscosity over a distance h_2, comparable with the distance h_1, should occur at the sea surface (Figure 2, profile (B)).

In the case of a stratified sea region where stratification is produced by temperature differences (a thermocline) or density differences (a pycnocline), the turbulence and hence the eddy viscosity are assumed to be reduced within the pycnocline (thermocline), giving the viscosity profile shown in Figure 2, profile (C). In this profile the tidal viscosity is reduced significantly from a value μ_s below the pycnocline to a value μ_u above it, over the pycnocline thickness h_p, with the centre of the pycnocline located at a distance d above the seabed (Figure 2, profile (C)).

2.7. *Time integration method*

Considering equation (18) with $\partial P/\partial x$ and F_e externally specified functions, a single-step, two-time-level integration method with time step τ takes the form

$$\frac{U_r^{t+\tau}-U_r^t}{\tau}=\frac{\partial P^{(t+\theta\tau)}}{\partial x}a_r+F_e-\frac{\alpha^{(t+\beta\tau)}}{h^2}\varepsilon_r[(1-\theta)u_r^t+\theta u_r^{t+\tau}], \tag{25}$$

with θ a weighting in the range $0\leqslant\theta\leqslant1$ and β a similar weighting. Obviously with $\theta=0$ we obtain an explicit time integration method which requires the time step τ to satisfy the stability condition[19,20]

$$\tau\leqslant 2h^2/\alpha\varepsilon_r, \tag{26}$$

which is computationally prohibitive in shallow water.

By time centring the viscosity term with $\theta = 0{\cdot}5$, an unconditionally stable integration scheme can be obtained if $\alpha^{(t+\beta\tau)}$ is time-invariant.[19,20] However, in many of the calculations performed later, $\alpha^{(t+\beta\tau)}$ is determined by the depth-mean currents $\bar{u}$ and $\bar{v}$ computed from

$$\bar{u} = \int_0^1 \psi_u \, d\sigma + \sum_{r=1}^{m} u_r \phi_r \bar{f}_r, \tag{27}$$

$$\bar{v} = \int_0^1 \psi_v \, d\sigma + \sum_{r=1}^{m} u_r \phi_r \bar{f}_r, \tag{28}$$

with

$$\bar{f}_r = \int_0^1 f_r \, d\sigma.$$

The alternative formulation is the calculation of $\alpha^{(t+\beta\tau)}$ from U_*, the frictional velocity given by

$$U_* = (\tau_B/\rho)^{1/2}, \tag{29}$$

with τ_B the total bed stress,

$$\tau_B = [(\tau_B^x)^2 + (\tau_B^y)^2]^{1/2}, \tag{30}$$

where τ_B^x and τ_B^y are given by equations (7b).

Obviously a flow-dependent eddy viscosity or one determined by U_* introduces a non-linearity in (25). This non-linearity is physically important; as shown by Davies,[24] it is responsible for generating the higher harmonics in a numerical model with a no-slip bottom boundary condition. The computational consequence of this non-linearity is that if β is non-zero, a non-linear problem has to be solved at each time step, which is computationally impractical. Consequently, in all calculations considered later, β was set to zero, i.e. the viscosity term was evaluated using the current or frictional velocity (U_*) at the lower time step.

In general θ was set to $\theta = 0{\cdot}5$, although as we will show later (see Section 3.3 for numerical examples), in shallow water with high viscosity this could produce an instability, particularly with a frictional-velocity- (U_*-) dependent viscosity. The simple explicit stability criterion suggests that instability due to the viscosity term for a given time step will increase with decreasing water depth and/or increasing viscosity. Such a finding appears to be borne out in practice, in that Davies[18] experienced numerical instabilities in very shallow water using a U_*-dependent viscosity with a no-slip condition in a three-dimensional model of the Irish Sea. This non-linear instability could, however, be removed by setting $\theta = 1$.

Since the frictional-velocity-dependent viscosity depends upon μ_0 (the bed viscosity at the previous time step) through equations (7b), it was necessary in this calculation to set a low background viscosity, namely $\mu_B = 0{\cdot}000\,01\ m^2\,s^{-1}$, when the calculation was started from rest in order to generate a bed stress. Also, since the value of U_* depends on the vertical derivative of the function at the seabed through equations (7b), then, as we will show later, it is essential to determine this bed derivative accurately.

2.8. Time-varying eddy viscosity

In the case of a time-varying flow-related eddy viscosity the viscosity is written as (equation (10))

$$\mu = \alpha(t)\Phi(\sigma),$$

with

$$\Phi(\sigma) = V(\sigma) \Big/ \int_1^0 V(\sigma) \mathrm{d}\sigma \tag{31}$$

a normalized viscosity profile determining the vertical variation in μ from the specified function $V(\sigma)$ (Figure 2).

In the case of a U_*-dependent viscosity (equation (22)) α is given by

$$\alpha = K_* K_0 U_*, \tag{32}$$

where K_* is an arbitrary constant determining the depth-mean value of viscosity, with the bed viscosity depending on the ratios $\mu_0 : \mu_1$ (Figure 2, profile (A)), etc. used in the calculation.

Similarly, in the case of $\bar{u}$ (equation (23)) or $\bar{u}^2$ (equation (24)) α is given by

$$\alpha = K_1 h \bar{u} \tag{33}$$

or

$$\alpha = K_2 \bar{u}^2 / \omega. \tag{34}$$

3. NUMERICAL CALCULATIONS IN A HOMOGENEOUS SEA

3.1. Constant-pressure-driven flow, $h = 10$ m, no external function

In an initial series of calculations, rotational effects were neglected, i.e. $\gamma = 0$, and eddy viscosity profile (A) (Figure 2) was used with $\mu_1 = 0{\cdot}1\ \mathrm{m^2\,s^{-1}}$, $\mu_0 = 0{\cdot}0002\ \mathrm{m^2\,s^{-1}}$ and $h_1 = 0{\cdot}1\ h$, i.e. a time-invariant viscosity, and a water depth $h = 10$ m. Motion was started from rest by a suddenly applied and maintained pressure gradient $\partial P/\partial x = 1 \times 10^{-4}\ \mathrm{m\,s^{-2}}$, $\partial P/\partial y = 0$ and the model was integrated forwards in time until a steady state, i.e. $\partial u/\partial t = 0$, was obtained. Since rotational effects were neglected and $\partial P/\partial y = 0$, the v-component of velocity remained zero.

For the problem considered here, the surface stress was zero and $\gamma = 0$; then by integrating equation (1) through the vertical, it is easy to show that in the steady state the bed stress term $\tau_B^x/\rho h$ must balance the external pressure gradient term. By this means it is possible to determine the accuracy of the bed stress computed with the modal expansion. As we will show later, the determination of an accurate bed stress is particularly important with a U_*-dependent viscosity.

In an initial series of calculations, modes were computed using 50 knots in the vertical and a range of knot distributions based on a logarithmic transformation (Table I, knot distributions A, B and C).

If a coarse knot spacing (Table I, knot distribution C) is used at the bed, then the high-shear region is not adequately resolved and appears as a more gradual change similar to that found with a higher μ_0-value. In essence, the effect of computing modes with a coarse knot spacing in the near-bed region is to artificially increase the μ_0-value.

Profiles of the first few modes computed with knot distribution A are shown in Figure 3. Each mode is normalized to unity at the sea surface and is zero at the seabed. A high-shear near-bed region is clearly evident in the figure, with the shear decreasing as the bed eddy viscosity increases (compare profiles 1 and 2, Figure 3).

The steady state surface and mid-depth currents together with the bed stress term as the number of modes, M, in expansions (7a) is increased are shown in Table II. (In this series of calculations the external functions ψ_u and ψ_v were zero.) Table II shows that with knot distribution A the bed stress term rapidly converges towards its exact value of -1×10^{-4}, with the currents at all depths showing a similar rate of convergence. With knot distribution B, i.e.

Table I. Knot distributions used to compute the modal basis set

Knot distribution	Knot spacing
A	Logarithmic distribution with $S_o = 5{\cdot}0 \times 10^{-6}$
Ā	Logarithmic distribution with $S_o = 5{\cdot}0 \times 10^{-8}$
B	Logarithmic distribution with $S_o = 5{\cdot}0 \times 10^{-4}$
C	Logarithmic distribution with $S_o = 5{\cdot}0 \times 10^{-2}$
D	Specified vertical spacing
A*	Log–linear distribution with $S_* = 0{\cdot}9$, $S_o = 2{\cdot}0 \times 10^{-8}$
B*	Log–linear distribution with $S_* = 0{\cdot}9$, $S_o = 5{\cdot}0 \times 10^{-4}$
C*	Log–linear distribution with $S_* = 0{\cdot}9$, $S_o = 5{\cdot}0 \times 10^{-2}$
B1	As knot distribution B in the near-bed region, with a spacing $\Delta\sigma = 0{\cdot}0002$ in the pycnocline
B2	As knot distribution B1, but with a spacing $\Delta\sigma = 0{\cdot}02$ in the pycnocline

a coarser knot spacing in the near-bed region, the currents at all depths converge rapidly, giving identical values to those found with knot distribution A. Although the bed stress converges to a value 10% below its exact value, this does not appear to influence the convergence of the currents with this formulation of the eddy viscosity. However, with a coarser near-bed knot spacing (knot distribution C), not only is the bed stress in the model severely underestimated, but the currents at various depths converge to a value below the correct one (Table II, knot distribution C). The lack of near-bed resolution means that the eigenvalues are not computed correctly (see Table III) and this influences the steady state current profile.

Table III shows that the first eigenvalue computed with the coarse knot spacing at the bed (knot distribution C) is approximately 20% higher than those determined with other knot spacings. This effectively increases the viscosity in the solution. Similar errors, but with a reduced magnitude (of the order of 5% in the fifth mode), are evident for the higher eigenvalues (Table III), although the higher modes contribute less to the solution and hence the errors in the magnitude of these eigenvalues are less important.

In the case of knot distributions A and B there is a very fine spacing in the near-bed region with a much coarser spacing above this. To check that the coarser resolution in the upper part of the water column did not influence the solution, the calculation was repeated with knot distribution D with over 60 knots in the vertical and a fine distribution in the near-bed region, comparable with knot distribution A, together with a fine distribution comparable with knot distribution C in the upper part. The currents, bed stresses and eigenvalues computed with this distribution (Tables II and III) are comparable with those of knot distributions A and B. The current profiles show a very-high-shear near-bed region with a more gradual near-linear variation above this (see later results). The nature of this profile and the results of the calculations suggest that it is essential to use a set of knots with a very high resolution in the near-bed region when the eddy viscosity is low in order to resolve the rapidly changing profile in this area. Above the near-bed region a coarser distribution can be applied. The use of a logarithmic or log–linear transformed spacing to achieve this appears optimal.

Although knot distribution C was inadequate when $\mu_0 = 0{\cdot}0002\ \mathrm{m^2\,s^{-1}}$, such a distribution should be accurate for higher μ_0-values, because increasing μ_0 reduces the bed shear. This assumption was tested using both knot distributions A, B and C based on logarithmic spacing and knot distributions A*, B* and C* based on a log-linear spacing (Table I), with $\mu_0 = 0{\cdot}0002\ \mathrm{m^2\,s^{-1}}$ (calculation 1) and increased to $\mu_0 = 0{\cdot}002\ \mathrm{m^2\,s^{-1}}$ (calculation 2). The steady

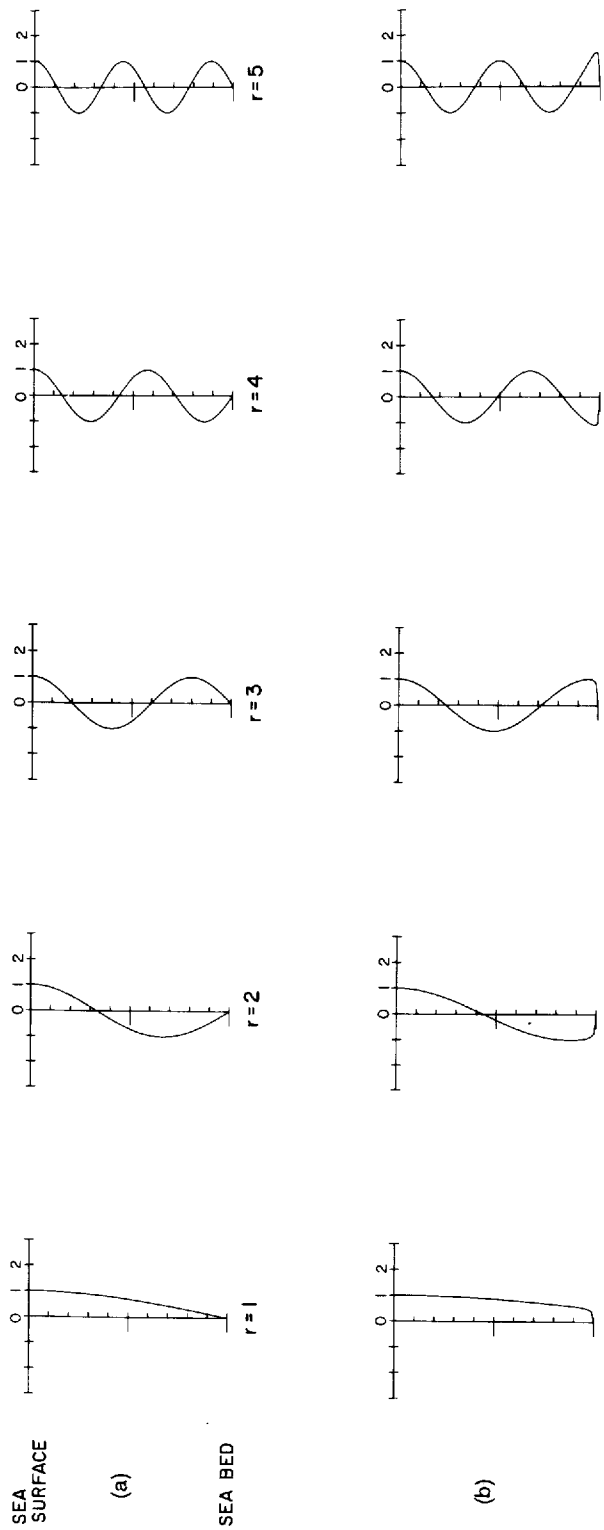

Figure 3. Vertical profiles of the first five modes computed using viscosity profile (A) with (a) $\mu_0=\mu_1=$ constant and (b) $\mu_1=0{\cdot}1\ \mathrm{m^2\,s^{-1}}$, $\mu_0=0{\cdot}0001\ \mathrm{m^2\,s^{-1}}$, $h_1=0{\cdot}9h$

Table II. Values of surface ($\sigma=0$) and mid-depth ($\sigma=0{\cdot}5$) velocities (cm s^{-1}) and bed stress as a function of number of modes M, in expansions (7a), with $\psi_u=\psi_v=0$, using modes computed for knot distributions A, $\bar{A}$, B, C and D, in a water depth $h=10$ m, with a time-invariant eddy viscosity

	Number of modes, M			
	1	2	4	6
	Knot distribution A			
$u(\sigma=0)$	−10·34	−10·16	−10·18	−10·18
$u(\sigma=0{\cdot}5)$	−8·90	−8·94	−8·93	−8·93
$\tau_B^x/\rho h\times 10^4$	−0·960	−0·990	−0·996	−0·998
	Knot distribution $\bar{A}$			
$u(\sigma=0)$	−10·34	−10·16	−10·17	−10·18
$u(\sigma=0{\cdot}5)$	−8·90	−8·95	−8·92	−8·93
$\tau_B^x/\rho h\times 10^4$	−0·960	−0·990	−0·996	−0·998
	Knot distribution B			
$u(\sigma=0)$	−10·34	−10·16	−10·17	−10·18
$u(\sigma=0{\cdot}5)$	−8·90	−8·95	−8·92	−8·93
$\tau_B^x/\rho h\times 10^4$	−0·867	−0·895	−0·900	−0·902
	Knot distribution C			
$u(\sigma=0)$	−8·36	−8·17	−8·19	−8·19
$u(\sigma=0{\cdot}5)$	−6·89	−6·96	−6·94	−6·94
$\tau_B^x/\rho h\times 10^4$	−0·042	−0·044	−0·044	−0·044
	Knot distribution D			
$u(\sigma=0)$	−10·34	−10·16	−10·18	−10·18
$u(\sigma=0{\cdot}5)$	−8·90	−8·95	−8·93	−8·93
$\tau_B^x/\rho h\times 10^4$	−0·959	−0·990	−0·996	−0·998

Table III. Influence of knot distribution on first, second and fifth eigenvalues

Knot distribution	Eigenvalue		
	1	2	5
A	0·81045	13·475	152·004
B	0·81047	13·475	151·650
C	1·00801	14·339	158·300
D	0·81045	13·475	151·616

state currents computed with 10 modes based on these knot distributions are shown in Table IV. It is clear that the currents are not significantly different in calculation 2, although the bed stress value computed using knot distributions C and C* is significantly underestimated. The log–linear spacing of knot distribution C*, although coarse in the near-bed region, does for a given number of knots provide more resolution in the upper part of the water column, which as we will show is important when stratification is present (see later).

Table IV. Computed surface ($\sigma=0$) and mid-depth ($\sigma=0{\cdot}5$) velocities (cm s^{-1}) and bed stress using 10 modes based on knot distributions A, B, C, A*, B* and C*, using viscosity profile (A), with $\mu_1=0{\cdot}1\ m^2\ s^{-1}$, $\mu_0=0{\cdot}0002\ m^2\ s^{-1}$ (calculation 1) and $\mu_1=0{\cdot}1\ m^2\ s^{-1}$, $\mu_0=0{\cdot}002\ m^2\ s^{-1}$ (calculation 2)

	Logarithmic distribution			Log–linear distribution		
	A	B	C	A*	B*	C*
			Calculation 1			
$u(\sigma=0)$	−10·18	−10·18	−8·19	−10·18	−10·18	−8·18
$u(\sigma=0{\cdot}5)$	−8·93	−8·93	−6·94	−8·93	−8·93	−6·93
$\tau_B^x/\rho h\times 10^{-4}$	−0·998	−0·902	−0·044	−0·998	−0·898	−0·043
			Calculation 2			
$u(\sigma=0)$	−7·95	−7·95	−7·61	−7·95	−7·95	−7·62
$u(\sigma=0{\cdot}5)$	−6·70	−6·70	−6·37	−6·69	−6·69	−6·36
$\tau_B^x/\rho h\times 10^{-4}$	−0·999	−0·996	−0·340	−0·997	−0·996	−0·337

Table V. Computed surface ($\sigma=0$), mid-depth ($\sigma=0{\cdot}5$) and near-bed ($\sigma=0{\cdot}95$) velocities (cm s^{-1}) and bed stress using 10 modes determined from knot distributions A and B, with viscosity computed from $h\bar{u}$ (calculation 1), $\bar{u}^2$ (calculation 2) and U_* (calculation 3)

	Calculation 1		Calculation 2		Calculation 3	
	A	B	A	B	A	B
$u(\sigma=0)$	−68·20	−68·19	−41·19	−41·19	−743·2	−778·5
$u(\sigma=0{\cdot}5)$	−59·82	−59·81	−36·14	−36·13	−651·9	−682·9
$u(0{\cdot}95)$	−36·76	−36·75	−22·20	−22·19	−400·6	−419·6
$\tau_B^x/\rho h\times 10^{-4}$	0·999	0·903	0·999	0·903	0·999	0·903

Obviously in a series of calculations in which the eddy viscosity remains independent of the flow, any errors in the flow field do not feed back to the calculation through the eddy viscosity and hence compound the error in the total solution. However, physically the viscosity should depend on the flow in terms of either $h\bar{u}$ (equation (23)), $\bar{u}^2$ (equation (24)) or U_* (equation (22)).

To examine the influence of knot resolution with a flow-dependent viscosity, the previous series of calculations were repeated using viscosity profile (A) with a $\mu_1:\mu_0$ ratio of 0·1–0·0002, $K_1=0{\cdot}0025$ (equation (23)) (calculation 1), $K_2/\omega=0{\cdot}2$ (equation (24)) (calculation 2) and $K_*=5$ (equation (22)) (calculation 3). The steady state bed stresses and currents computed with knot distributions A and B and these various flow-dependent viscosity formulations are given in Table V. The currents at various depths computed using 10 modes based on knot distributions A and B by calculations 1 and 2 ($h\bar{u}$ or $\bar{u}^2$-dependent viscosity) are not significantly different despite a 10% difference in bed stress. However, the currents computed with a U_*-dependent viscosity (calculation 3) are of the order of 5% higher with knot distribution B than with distribution A. This can presumably be attributed to the lower viscosity due to the lower bed stress and hence U_* with knot distribution B. As demonstrated previously, the coarser the knot spacing in the near-bed region, the lower is the bed stress and hence the greater is the error in any solution using a U_*-dependent viscosity. In the next subsection we will examine whether the addition of an external function can improve the near-bed shear stress when the modes are computed using a coarse knot spacing.

3.2. Constant-pressure-driven flow, $h = 10$ m, with an external function

In this series of calculations we again use viscosity profile (A) with $\mu_1 = 0{\cdot}1\ \mathrm{m^2\,s^{-1}}$, $\mu_0 = 0{\cdot}0002\ \mathrm{m^2\,s^{-1}}$ and $h_1 = 0{\cdot}1\ h$. Also, a water depth $h = 10$ m with $\partial P/\partial x$ as before, $\partial P/\partial y = 0$ and $\gamma = 0$ was employed. The steady state currents and bed stress magnitudes computed using 10 modes determined from knot distributions A, B and C, initially with no external function and then with a range of external function scaling parameters, are shown in Table VI.

Consider initially the solution based on modes computed with knot distribution C. Adding an external function with $E_s = 0{\cdot}0001$ and $\lambda = 1$ slightly improves the bed stress value, while increasing λ to 10 leads to a significant improvement in the bed stress, although there is now a significant error in the computed currents. Decreasing E_s to 0·00001 with $\lambda = 1$ also improves the bed stress, although again there is an appreciable error in the computed currents. An external function with these parameters improves the accuracy of the bed stress computed using modes determined from knot distribution B, although again there is a significant error in the computed velocity. A similar error in velocity occurred with modes based on knot distribution A.

These calculations suggest that the addition of an external logarithmic function with carefully chosen E_s and λ can certainly improve the accuracy of the bed stress computed using a modal expansion based on a coarse knot spacing, although the accuracy of the current may be reduced. The major problem of adding an external function of a logarithmic nature is how to decide upon the choice of E_s and λ. Obviously in the present case when the bed stress is known, optimal E_s and λ could be chosen. In a more realistic calculation it would be impossible to make the optimal choice and the consequence of choosing inappropriate values of E_s and λ would be erroneous answers. Since the modes are computed only once prior to the integration of the hydrodynamic equations, a better alternative to the application of an external function would appear to be the accurate determination of the modes using a large number of knots with a logarithmic or

Table VI. Computed surface ($\sigma = 0$) and mid-depth ($\sigma = 0{\cdot}5$) velocities ($\mathrm{cm\,s^{-1}}$) and bed stress determined using 10 modes based on knot distributions A, B and C, initially with no external function, then with an external function using a range of scaling parameters λ and E_s

	No external function	$\lambda = 1$ $E_s = 0{\cdot}0001$	$\lambda = 10$ $E_s = 0{\cdot}0001$	$\lambda = 1$ $E_s = 0{\cdot}00001$
	Knot distribution A			
$u(\sigma = 0)$	−10·18	−9·12	0·41	−8·86
$u(\sigma = 0{\cdot}5)$	−6·13	−5·33	1·82	−5·07
$\tau_B^x/\rho h \times 10^4$	−0·999	−0·899	+0·035	−1·012
	Knot distribution B			
$u(\sigma = 0)$	−10·18	−9·12	0·40	−8·86
$u(\sigma = 0{\cdot}5)$	−6·13	−5·33	1·81	−5·08
$\tau_B^x/\rho h \times 10^4$	−0·903	−0·811	+0·095	−0·936
	Knot distribution C			
$u(\sigma = 0)$	−8·19	−7·40	−0·31	−7·38
$u(\sigma = 0{\cdot}5)$	−4·14	−3·02	1·10	−3·60
$\tau_B^x/\rho h \times 10^4$	−0·044	−0·059	−0·196	−0·239

log–linear spacing and a small value of s_0 chosen so that the knot transformation ensures that the modes are accurately determined in the near-bed high-shear layer.

3.3. *Constant-pressure-driven flow, $h=1$ m, no external function*

In the previous series of calculations the viscosity term was centred in time and the solution did not exhibit any signs of numerical instability with a time step of 360 s. However, as demonstrated earlier, if a flow-dependent viscosity is used, there exists the possibility of a non-linear-type instability, since the flow-dependent viscosity is evaluated at a lower time step.

To examine this problem, the previous series of calculations were repeated with no external function, a $\mu_1:\mu_0$ ratio of 0·1–0·0002 and the eddy viscosity computed in terms of $h\bar{u}$ with $K_1=0{\cdot}0025$ (calculation 1), $\bar{u}^2$ with $K_2/\omega=0{\cdot}2$ (calculation 2) and U_* with $K_*=5$ (calculation 3), with modes based on knot distributions A, B and D and θ-values of 0·5 or 1. The currents at a number of depths and bed stresses computed using an expansion of 10 modes based on these knot distributions are shown in Table VII. In practice the solutions with the eddy viscosity time centred ($\theta=0{\cdot}5$) and at the higher time step ($\theta=1$) were both found to be stable, with no differences in current magnitudes. In the case of calculations 1 and 2 all three knot distributions yielded identical flow fields, although the bed stress with knot distribution B was underestimated by 10%. In the case of the U_*-dependent flow field some slight differences in current were found (Table VII).

When μ_1 was increased to 10, a significant time step oscillation was obtained when $\theta=0{\cdot}5$, which disappeared when $\theta=1$ (Table VIII), suggesting that for flow-dependent viscosities in shallow water a value of $\theta=1$ significantly enhances the stability of the solution, a finding consistent with that of Davies.[18] As in the previous series of calculations, the modes determined using a coarse knot spacing in the near-bed region (knot distribution C) significantly underestimate the bed shear stress (Table VIII).

Table VII. Computed currents (cm s^{-1}) and bed stress in a water depth $h=1$ m using 10 modes determined from knot distributions A, B and D, with viscosity computed from $h\bar{u}$ (calculation 1), $\bar{u}^2$ (calculation 2) and U_* (calculation 3)

	$u(\sigma=0)$	$u(\sigma=0{\cdot}5)$	$u(\sigma=0{\cdot}95)$	$\tau_B^x/\rho h\times 10^4$
		Calculation 1		
A	−21·56	−18·92	−11·62	−0·9990
B	−21·56	−18·92	−11·62	−0·9027
D	−21·56	−18·92	−11·62	−0·9989
		Calculation 2		
A	−8·87	−7·79	−4·78	−0·9990
B	−8·87	−7·78	−4·78	−0·9027
D	−8·87	−7·78	−4·78	−0·9989
		Calculation 3		
A	−20·15	−17·68	−10·86	−0·9992
B	−20·97	−18·39	−11·30	−0·9027
D	−20·15	−17·68	−10·86	−0·9989

Table VIII. Computed currents and bed stress (using a U_*-dependent viscosity) with $h=1$ m at consecutive time steps t and $t+\tau$ at near-steady state, determined with viscosity time-centred (calculation 1) and evaluated at the higher time step (calculation 2) using various knot distributions

	Calculation 1		Calculation 2	
	t	$t+\tau$	t	$t+\tau$
	Knot distribution A			
$u(\sigma=0)$	−0·31	−0·10	−0·39	−0·39
$u(\sigma=0{\cdot}5)$	−0·31	−0·07	−0·36	−0·36
$u(\sigma=0{\cdot}95)$	−0·51	0·23	−0·27	−0·27
$\tau_B^x/\rho h\times 10^4$	2·24	−4·63	−0·897	−0·897
	Knot distribution C			
$u(\sigma=0)$	−1·71	−1·39	−1·53	−1·53
$u(\sigma=0{\cdot}5)$	−1·56	−1·24	−1·38	−1·38
$u(\sigma=0{\cdot}95)$	−1·55	−0·81	−0·97	−0·97
$\tau_B^x/\rho h\times 10^4$	−0·028	−0·058	−0·042	−0·042
	Knot distribution D			
$u(\sigma=0)$	−0·45	−0·00	−0·37	−0·37
$u(\sigma=0{\cdot}5)$	−0·39	−0·02	−0·34	−0·34
$u(\sigma=0{\cdot}95)$	−0·47	0·17	−0·25	−0·25
$\tau_B^x/\rho h\times 10^4$	1·61	−4·30	−0·9998	−0·9998

4. NUMERICAL CALCULATIONS IN A STRATIFIED SEA

4.1. Modal structure

In the previous series of calculations we considered eddy viscosity profiles characteristic of well-mixed homogeneous sea regions. The calculations clearly showed that the vertical profiles of currents and associated modes were characterized by a high-shear near-bed region with a more gradually varying profile above it. In this case eigenfunctions (modes) could be accurately computed using a logarithmic or log–linear knot spacing provided that a high resolution was maintained in the near-bed region. For a fixed number of knots, high resolution in the near-bed region obviously gives rise to poorer resolution above this layer. In the case of a homogeneous flow this is not particularly important, since the current only varies slowly through the vertical in the upper part of the water column.

However, for the case of tidal flow in a stratified sea the influence of the stratification is to reduce the tidal turbulence in the upper part of the water column, giving rise (as will be shown later) to a high-shear layer coinciding with the region of the water column (the pycnocline) where eddy viscosity is reduced. Consequently it is necessary to use a set of modes based on a knot distribution which can resolve this high-shear region as well as the near-bed shear layer.

Typically stratification caused by thermal effects (heating at the sea surface) in a tidally dominated region such as the North Sea occurs in water depths of the order of 50 m or deeper, with tidal currents of the order of 50 cm s^{-1} or less. In shallower water or with stronger tidal currents, tidally induced turbulence produced at the seabed will normally mix the water column,

removing any effects of stratification. Although the primary aim of this paper is to examine numerical problems associated with a no-slip bottom boundary condition and the presence of mid-water stratification, we will subsequently consider the physical effects of stratification on tidal currents. For this reason we have chosen physically realistic values of water depth $h = 50$ m and tidal current strength (see later).

In an initial series of calculations to determine an optimal knot distribution in a stratified water column, water depth $h = 50$ m, stratification was assumed to occur at mid-water, $d = 25$ m (Figure 2, profile (C)), with $h_p = 1$ m (a sharp pycnocline) and $h_1 = 2$ m. Viscosity values of $\mu_0 = 0{\cdot}0001$, $\mu_s = 0{\cdot}1$ and $\mu_u = 0{\cdot}0001$ m^2 s^{-1} were used in the vertical. A low value of μ_u corresponds to an intense stable pycnocline which inhibits tidal turbulence in the upper part of the water column.

The first four modes computed using knot distribution $\bar{A}$ with viscosity profile (C) (Figure 2) are shown in Figure 4 profile (a). Although this distribution is ideal for computing modes in the case of a single high-shear bottom boundary layer, there are very few knots in the region of the pycnocline and the upper half of the water column and hence the high-shear layer associated with the pycnocline is not resolved. Also, it is clearly evident from Figure 4, profile (a) that there are a number of spurious 'ripples' in the eigenfunction profiles. Using knot distribution A gives a coarse, but still satisfactory distribution of knots in the near bed-region (see bed stresses in Table II), but with better resolution in the upper part of the water column. The first four modes computed with this knot distribution are shown in Figure 4, profile (b). A comparison of profiles (a) and (b) shows that the number of ripples in the first few modes is reduced; however, physically unrealistic ripples occur in the fourth mode.

Improved resolution in the upper part of the water column can obviously be obtained using knot distribution B, which is also satisfactory in the near-bed region (Table II). However, this still does not have enough resolution within the pycnocline. This problem can be overcome by using knot distribution B in the bottom 30–40 m of the water column, below the pycnocline, with a uniform fine knot spacing above this, or a telescoping knot spacing with its finest grid (grid spacing $\Delta\sigma = 0{\cdot}0002$) in the centre of the pycnocline (knot distribution B1).

The first four modes computed with this knot distribution are shown in Figure 4, profile (c). It is evident from a comparison of profiles (b) and (c) that it is essential to have high resolution in the region of the pycnocline if the associated high-shear region is to be resolved. Obviously adding a refined knot distribution within the pycnocline whilst maintaining a logarithmic distribution in the near-bed region increases the total number of knots in the case of knot distributions B and B1 from 50 knots to over 100 knots. However, since the modes are computed prior to integrating the hydrodynamic equations, the computational overhead is small.

The accuracy of the various knot distributions in computing tidal amplitude and phase will be considered in the next subsection.

4.2. Tidal calculations

In this series of calculations the motion was driven by a pressure forcing of 12 h period (tidal period) in the x-direction, with $h_x = 0{\cdot}2$ (chosen to give an inviscid flow of the order of 50 cm s^{-1}) and $h_y = 0$. Since rotational effects are important in determining tidal current profiles, a value of $\gamma = 0{\cdot}00012$ s^{-1} (a value used previously by Davies[21]), appropriate to the latitude of the North Sea, was used. The hydrodynamic equations were integrated forwards in time until the effects of the initial conditions of zero motion had been removed and a periodic solution was obtained which was then Fourier analysed to give the amplitude and phase of the u- and v-components of velocity at a number of depths.

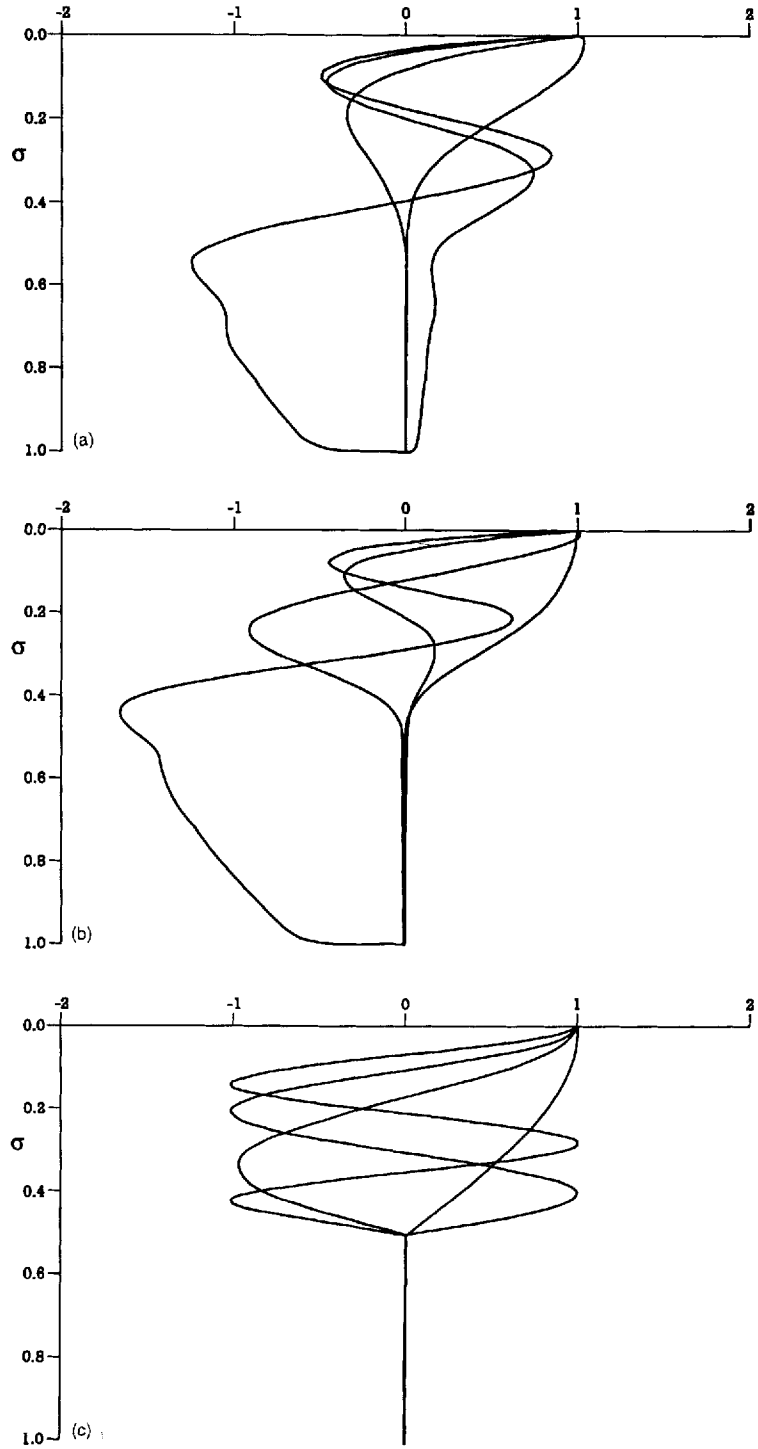

Figure 4. Vertical variation of the first four modes in a stratified region computed with (a) knot distribution $\bar{A}$, (b) knot distribution A and (c) knot distribution B1

In an initial series of calculations to examine the modal convergence and the accuracy of the computed modes, an identical set of parameters to those used previously, namely $h=50$ m, $\mu_0=\mu_u=0{\cdot}0001\ \mathrm{m^2\,s^{-1}}$, $\mu_s=0{\cdot}1\ \mathrm{m^2\,s^{-1}}$, $d=25$ m, $h_p=1$ m and $h_1=2$ m, was employed.

This set of parameters corresponds to a very intense pycnocline which effectively suppresses tidal turbulence in the upper part of the water column. As such it provides a rigorous test of the modal expansion ability to resolve the high shear in the pycnocline region. Also, since the turbulence above the pycnocline is small, the computed surface current amplitudes and phases should correspond to their inviscid values of $h_u=0{\cdot}626\ \mathrm{m\,s^{-1}}$, $g_u=270°$, $h_v=0{\cdot}517\ \mathrm{m\,s^{-1}}$ and $g_v=180°$, which provides an independent test of the model's accuracy.

Profiles of the amplitude and phase of the u- and v-components of current computed using 10 modes based on knot distributions Ā, B2 and B1 are shown in Figure 5. Knot distributions B1

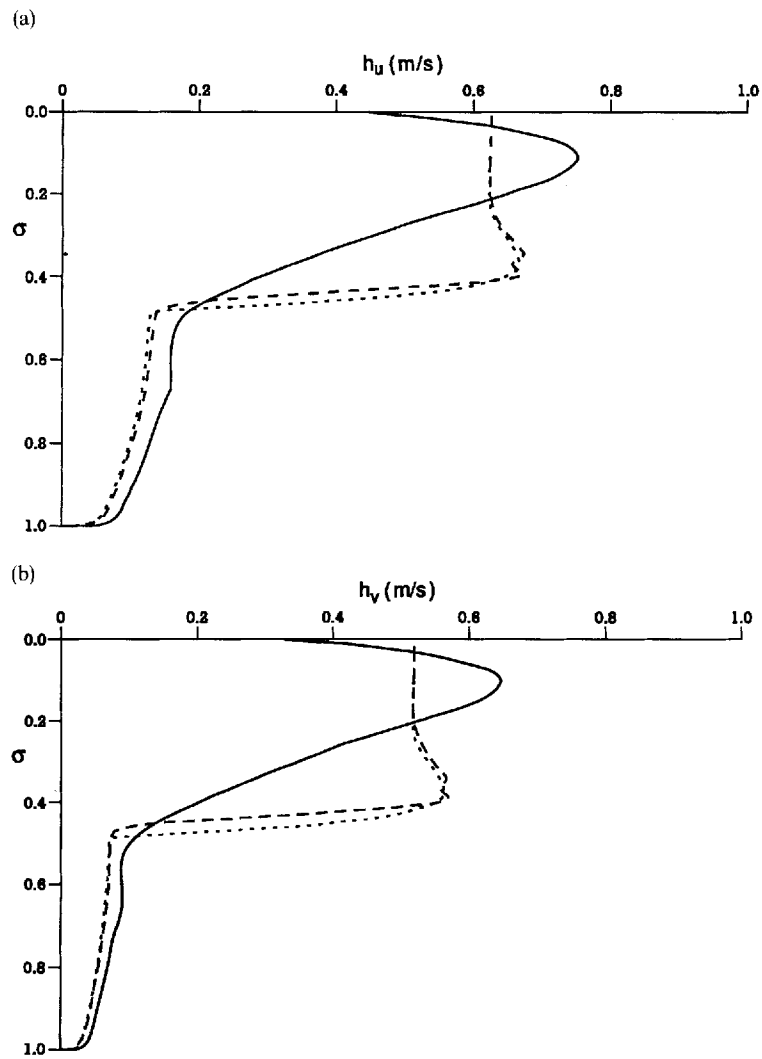

Figure 5. Profiles of tidal amplitude h_u, h_v ($\mathrm{m\,s^{-1}}$) and phase g_u, g_v computed with (a) knot distribution Ā (-), (b) knot distribution B2 (– – – –) and (c) knot distribution B1 (·····)

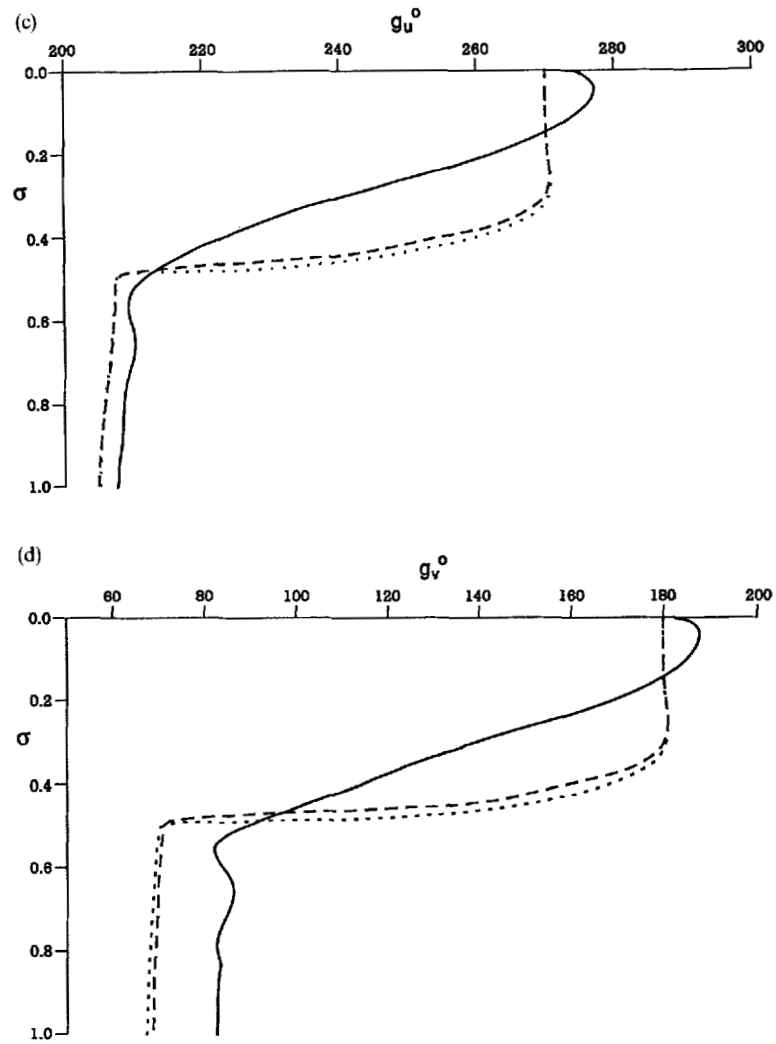

Figure 5. (Continued)

and B2 are identical to knot distribution centred within the pycnocline and the region above containing 10 knot intervals. In knot distribution B1 a fine knot spacing ($\Delta\sigma = 0{\cdot}0002$) is used within the pycnocline, with a coarser knot spacing ($\Delta\sigma = 0{\cdot}02$) used in knot distribution B2. The accuracy of this coarser knot spacing is considered later.

Clearly, as the number of knots within the pycnocline used to compute the modes increases, the spurious 'ripples' which are evident in Figure 5, profiles (a) (see in particular the phase g_v of the v-component of current) are reduced. However, there are still some spurious 'ripples' in the amplitude of the u- and v-components of velocity (Figure 5, profiles (b)) in the region above the pycnocline computed with knot distribution B2 (a coarse knot spacing in the pycnocline), although these are removed when the resolution is enhanced in this area (Figure 5, profiles (c), knot distribution B1).

It is also evident from Figure 5 that as the resolution in the pycnocline is improved, the abrupt change in current amplitude across the pycnocline is accurately resolved and the surface currents

reach their freestream values. This is clearly evident in Figure 5, profiles (c), where above the pycnocline in the upper 20% of the water column the current magnitude does not vary in the vertical and is shear-free.

This series of calculations has clearly illustrated the importance of using a high knot resolution both in the near-bed region and in the high-shear region across the pycnocline when computing the modes in order to accurately resolve these regions. Clearly, with inadequate resolution in the pycnocline (knot distribution B2), spurious oscillations occur, the pycnocline is not resolved accurately and there are significant errors in the computed currents.

In this calculation we have considered a very strong pycnocline to demonstrate problems associated with a lack of vertical resolution. In order to understand the role of μ_s and μ_u (Figure 2, profile (C)) in determining the current variation across the pycnocline, hence the shear and the required vertical resolution, it is instructive to consider the previous problem with a range of μ_u-values and thicknesses h_p of the pycnocline. In order to understand these results, it is necessary to consider initially the homogeneous situation (Figure 2, profile (A)) for two cases, namely $\mu_1 = 0{\cdot}0001\ \mathrm{m^2\,s^{-1}}$, the value of μ_u used in the previous calculation, and $\mu_1 = 0{\cdot}1\ \mathrm{m^2\,s^{-1}}$, the value of μ_s used earlier. In these calculations $\mu_o = 0{\cdot}0001\ \mathrm{m^2\,s^{-1}}$ with $h_1 = 0{\cdot}1h$ and $h = 50$ m.

Vertical profiles of h_u, g_u, h_v and g_v with $\mu_1 = 0{\cdot}0001\ \mathrm{m^2\,s^{-1}}$ are shown in Figure 6, profiles (a), with similar profiles for $\mu_1 = 0{\cdot}1\ \mathrm{m^2\,s^{-1}}$ in Figure 6, profiles (b). It is evident that with $\mu_1 = 0{\cdot}0001\ \mathrm{m^2\,s^{-1}}$ the current increases rapidly with height above the seabed, exceeds its freestream value and then falls to the freestream velocity. Calculations show that as μ_1 is increased, bed frictional effects extend further up the water column and the region of freestream flow is reduced. Eventually the portion of the water column where the freestream velocity is exceeded intersects the sea surface. Further increases in eddy viscosity give a reduced surface current, which falls below its freestream value (Figure 6, profiles (b)). Similar effects can be seen in the phase, which is reduced significantly below its freestream value (compare Figure 6, profiles (a) and (b)).

Figure 6 can be used to gain some insight into the nature of the processes producing the profiles of currents in the stratified case (Figure 5, profiles (c)). Considering initially the upper part of the profile shown in Figure 5, profiles (c), this is analogous to the lower half of Figure 6, profiles (a), since $\mu_s = \mu_1 = 0{\cdot}0001\ \mathrm{m^2\,s^{-1}}$ in both cases. In Figure 6, profiles (a) the high-shear bed layer is produced by the retarding force of bed turbulence; in Figure 5, profiles (c) it is produced by turbulence at the base of the pycnocline. Since the viscosity in both cases is low in the upper part of the water column, the profile above the pycnocline exhibits the characteristic 'overshoot', falling back to its freestream velocity. Below the pycnocline, since $\mu_s = \mu_1$, the velocity profile (Figure 5, profiles (c)) is analogous to the lower half of Figure 6, profiles (b), showing a high-shear bed region with a slowly increasing velocity above it. A similar explanation holds for the vertical variation of the phase.

Increasing the viscosity in the region above the pycnocline from $\mu_u = 0{\cdot}0001$ to $0{\cdot}0005\ \mathrm{m^2\,s^{-1}}$ reduces, as we would expect from Figure 6, the region of free stream flow (Figure 7, profiles (a)), while a further increase in viscosity to $\mu_u = 0{\cdot}01\ \mathrm{m^2\,s^{-1}}$ removes the region of free-stream flow and reduces the surface currents and phases below their freestream values (Figure 7, profiles (b)).

Maintaining these values of viscosity but increasing the thickness h_p to 15 m reduces the shear across the pycnocline, giving profiles of current amplitude and phase exhibiting little shear in the region of the pycnocline (Figure 7, profiles (c)). As h_p increases, both the surface current and phase are reduced below those found previously (compare Figure 7, profiles (c) and (b)).

Obviously, as h_p and μ_u are increased, the profile will tend towards that found for a homogeneous region (Figure 6, profiles (b)), with the surface current reduced below its freestream value and only a small phase difference between the sea surface and the seabed.

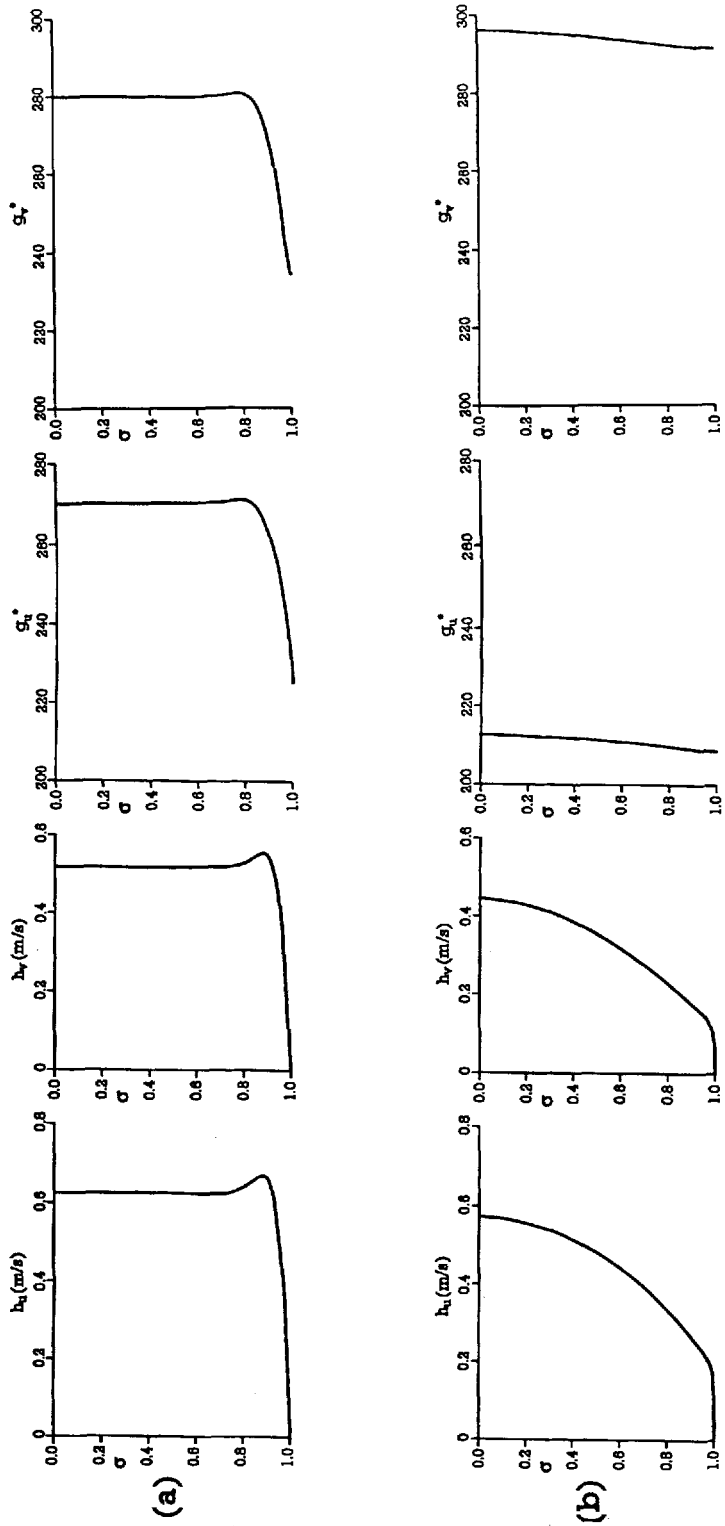

Figure 6. Profiles of tidal amplitude h_u, h_v ($m\,s^{-1}$) and phase g_u, g_v computed using viscosity profile (A) with (a) $\mu_1 = \mu_0 = 0{\cdot}0001\ m^2\,s^{-1}$ and (b) $\mu_1 = 0{\cdot}1\ m^2\,s^{-1}$, $\mu_0 = 0{\cdot}0001\ m^2\,s^{-1}$, $h_1 = 0{\cdot}1h$, with $h = 50$ m

The implications for the vertical knot resolutions used to compute the modes in this series of calculations can be clearly identified. (Similar implications using finite elements or a finite difference grid in the vertical also apply.) As in the homogeneous case, it is essential to maintain a high knot resolution in the bottom boundary layer when computing the modes in order to accurately resolve the near-bed shear layer. Obviously the greater the shear in this layer, the finer is the knot resolution required and the more important it is to use a logarithmic transformation. A logarithmic transformation giving the order of 10 knots in the bed shear layer would appear to be a necessary requirement. In a time-evolving problem in which the thickness of the bottom boundary layer increases or decreases and near-bed shear changes, the knot spacing should be sufficiently fine to resolve the largest shear likely to occur in the calculation if accuracy is to be maintained. Also, in the case of a sharp pycnocline, characterized by h_p of the order of a few metres and a significant difference between μ_u and μ_s (of the order of two orders of magnitude), it

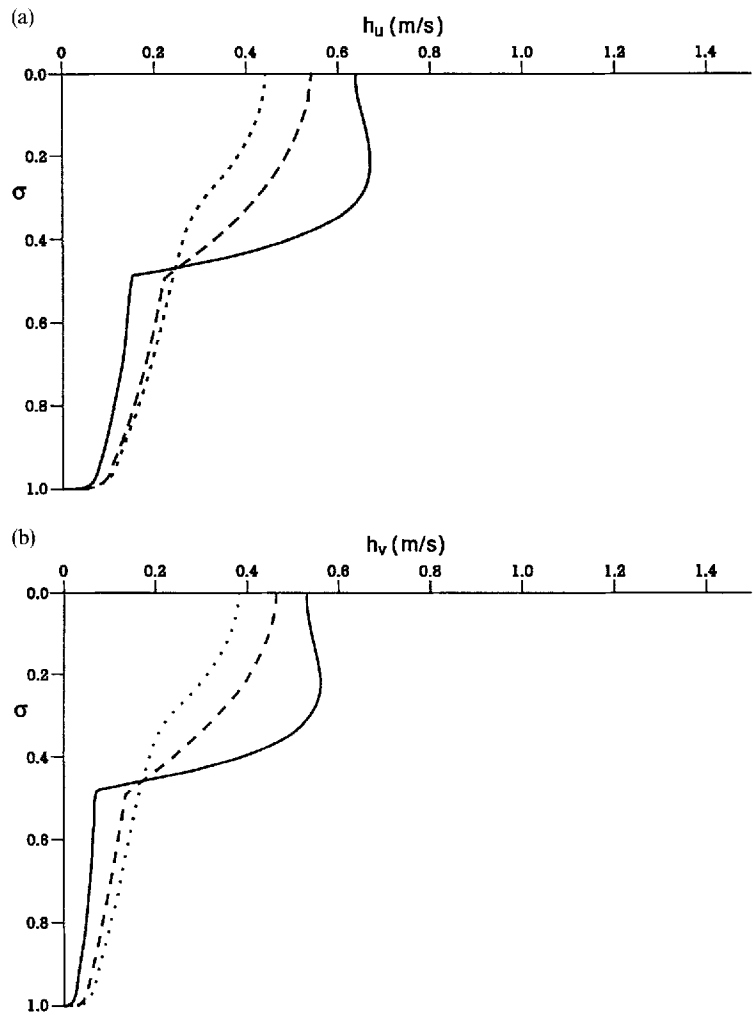

Figure 7. Profiles of tidal amplitude h_u, h_v ($m\,s^{-1}$) and phase g_u, g_v computed with (a) an intense pycnocline $\mu_u = 0{\cdot}0005\ m^2\,s^{-1}$, $h_p = 2$ m (——), (b) a weaker pycnocline, $\mu_u = 0{\cdot}01\ m^2\,s^{-1}$, $h_p = 2$ m (– – – –) and (c) a very diffuse pycnocline, $\mu_u = 0{\cdot}01\ m^2\,s^{-1}$, $h_p = 15$ m (·····)

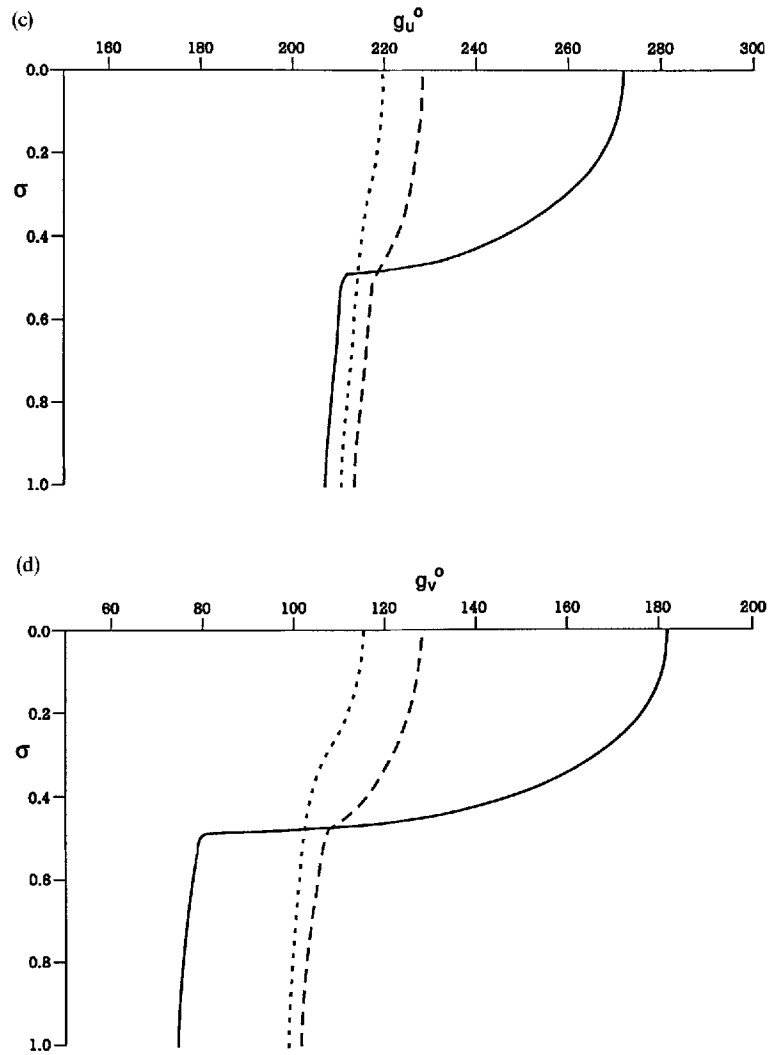

Figure 7. (Continued)

is essential to use a high knot resolution in the region of the pycnocline when computing the modes in order to maintain accuracy, but as the pycnocline weakens, the shear across it will diminish and the knot resolution can be reduced when the modes are computed. However, since the modes are only computed once and the time-consuming part of the calculation, namely the integration of the modes through time, is independent of the number of knots used to compute them, then there is not a major saving in computer time to be gained by reducing the number of knots.

It is important to note that the above conclusions concerning knot spacing are based on the use of fourth order B-splines (high-order elements). In the case of the more conventional second-order finite difference grid approach or low-order finite element method a higher resolution would be required to maintain this level of accuracy. In any time-stepping approach this would

have a high computational overhead in both computer time and memory. By using the modal approach developed here, high resolution is built into the modes and an accurate solution can be obtained with a small number of modes.

In the case of a flow-related eddy viscosity in a stratified region, as expected with a U_*-dependent viscosity, calculations show that it is essential to resolve the high-shear near-bed region. In the case of a $\bar{u}^2$- or $h\bar{u}$-dependent viscosity the resolution is of less importance, although it is necessary to ensure that there is sufficient resolution in the pycnocline region to accurately reproduce the depth-mean currents.

5. CONCLUDING REMARKS

By using the Galerkin method in the vertical with an expansion of basis functions, chosen as eigenfunctions (modes) of the eddy viscosity profile, a computationally economic means of resolving the high-shear bottom boundary layer can be obtained. Calculations show that the modal expansion converges rapidly and hence the method is computationally economic in terms of computer time and memory. However, it is essential to ensure that the modes are computed accurately, particularly in the near-bed region, if the modal expansion is to converge to the correct answer and the computed bed stress is to be accurately determined. A method of ensuring this, namely by computing the eigenfunctions (modes) using an expansion of B-splines with the knot spacing having a logarithmic or log–linear distribution, has been presented in this paper. Calculations illustrate that the alternative method of improving the accuracy of the expansion in the near-bed region using a mixed basis set involving a logarithmic function can give erroneous current profiles and bed stresses. Although this approach may be more successful with other basis functions, e.g. Legendre polynomials,[25] it appears essential to test the accuracy of any computed bed stress using the steady state pressure-driven flow problem presented here. Since the eigenfunctions are computed once, prior to the numerical integration of the hydrodynamic equations, there is little computational overhead in using a very fine knot distribution. This would not be so if an expansion of B-splines using a fine knot spacing or finite difference grid were used directly in the numerical integration, since then the computational overhead would be large.

Solutions computed with a flow-dependent eddy viscosity illustrate that the vertical resolution is important not only in determining the correct current profile but also in ensuring the appropriate eddy viscosity value which feeds back to the current profile. This is particularly important in the case of a no-slip condition with the viscosity computed from a frictional velocity. If the high-shear bottom boundary layer is not correctly resolved, then the frictional velocity is underestimated and an incorrect current profile is determined. In a model using a finite difference grid in the vertical a significant number of grid boxes, of the order of 50,[9,21] is required, leading to a heavy computational overhead. The present method avoids this problem, since once the modes have been computed, it is only necessary to store the modal coefficients, of the order of 10, at each horizontal grid point in a three-dimensional model. Since a modal model can be integrated with a time step identical to that used in a three-dimensional grid box model,[9] a saving of a factor of five to 10 in computer time and memory might be expected from a linear modal model compared with the same horizontal resolution finite difference model.

In the case of a flow-dependent eddy viscosity the viscosity term in the hydrodynamic equations is non-linear and the standard stability analysis cannot guarantee a stable solution. In shallow water, particularly with a frictional-velocity-dependent eddy viscosity centred in time, numerical instabilities can arise which rapidly mask the true solution in a three-dimensional simulation.[18] However, this problem is removed when the coefficients in the modal solution are evaluated at a higher time step.

For stratified flow, besides near-bed resolution, the accurate determination of the modal structure within the pycnocline is essential. Poor modal resolution gives erroneous results which do not reproduce the shear across the pycnocline and which exhibit spurious ripples. Obviously with a finite difference approach, high resolution in the near-bed region and within the pycnocline would involve a large computational effort which the modal method avoids. Calculations using an accurate set of modes clearly illustrate the importance of the pycnocline thickness and the viscosity both within and above the pycnocline in determining the profiles of current amplitude and phase.

Obviously in a three-dimensional calculation, if the stratification evolved in time to such an extent that the original choice of knot spacing could not resolve the new flow field and it was necessary to re-project the flow onto a new knot distribution and re-compute the modes, there would be a heavy computational penalty. However, in the majority of calculations this would not occur, and in any series of calculations in which the density field was treated diagnostically, the present approach would be computationally advantageous.

Further calculations using the modal approach developed in this paper to interpret results from recent field measurements of tidal profiles in stratified regions are in progress and will be reported in the oceanographic literature.

ACKNOWLEDGEMENTS

The care taken by Mr. R. A. Smith in preparing diagrams and Mrs. J. Hardcastle in typing the text is appreciated.

REFERENCES

1. A. M. Davies and G. Furnes, 'Observed and computed M_2 tidal currents in the North Sea', *J. Phys. Oceanogr.*, **10,** 237–257 (1980).
2. A. M. Davies, 'Application of the Galerkin method to the formulation of a three-dimensional nonlinear hydrodynamic numerical sea model', *Appl. Math. Modell.*, **4,** 245–256 (1980).
3. A. M. Davies, 'A three-dimensional model of the northwest European continental shelf with application to the M_4 tide', *J. Phys. Oceanogr.*, **16,** 797–813 (1986).
4. R. B. Gordon and M. L. Spaulding, 'Numerical simulations of the tidal- and wind-driven circulation in Narragansett Bay,' *Estuar., Coastal Shelf Sci.*, **24,** 611–636 (1987).
5. G. Furnes, 'A three-dimensional numerical sea model with eddy viscosity varying piecewise linearly in the vertical,' *Continental Shelf Res.*, **2,** 231–241 (1983).
6. J. N. Aldridge and A. M. Davies, 'A high resolution three dimensional hydrodynamic tidal model of the Eastern Irish Sea', *J. Phys. Oceanogr.*, in press.
7. A. M. Davies and J. E. Jones, 'A three dimensional model of the M_2, S_2, N_2, K_1 and O_1 tides in the Celtic and Irish Seas', *Progress in Oceanography*, **29,** 197–234 (1992).
8. A. M. Davies and J. E. Jones, 'A three-dimensional wind driven circulation model of the Celtic and Irish Seas', *Continental Shelf Res.*, **12,** 159–188 (1992).
9. A. M. Davies and J. E. Jones, 'Application of a three-dimensional turbulence energy model to the determination of tidal currents on the northwest European shelf', *J. Geophys. Res.*, **95,** 18,143–18,162 (1990).
10. A. M. Davies, 'Formulation of a linear three-dimensional hydrodynamic sea model using a Galerkin–eigenfunction method', *Int. j. numer. methods fluids*, **3,** 33–60 (1983).
11. A. M. Davies, 'Solution of the 3D linear hydrodynamic equations using an enhanced eigenfunction approach', *Int. j. numer. methods fluids*, **13,** 235–250 (1991).
12. R. W. Lardner, 'Numerical solution of the linearized three-dimensional tidal equations using eddy viscosity eigenfunctions', *J. Geophys. Res.*, **95,** (C12), 22,269–22,274 (1990).
13. T. J. Zitman, 'Quasi three-dimensional current modelling based on a modified version of Davies' shapefunction approach,' *Continental Shelf Res.*, **12,** 143–158 (1992).
14. A. M. Davies, 'Modelling currents in highly sheared surface and bed boundary layers', *Continental Shelf Res.*, **12,** 189–211 (1992).
15. K. F. Bowden, 'Physical problems of the benthic boundary layer', *Geophys. Surv.*, **3,** 255–296 (1978).
16. K. F. Bowden, L. A. Fairbairn and P. Hughes, 'The distribution of shearing stresses in a tidal current', *Geophys. J. R. Astronom. Soc.*, **2,** 288–305 (1959).

17. K. F. Bowden and S. R. Ferguson, 'Variations with height of the turbulence in a tidally-induced bottom boundary layer', in J. C. J. Nihoul (ed.), *Marine Turbulence, Proc. 11th Int. Liege Colloq. on Ocean Hydrodynamics*, 1979, Elsevier, Amsterdam, 1980, pp. 259–286.
18. A. M. Davies, 'A bottom boundary layer resolving three dimensional model: a sensitivity study of eddy viscosity formulation', *J. Phys. Oceanogr.*, in press.
19. A. M. Davies, 'Spectral models in continental shelf sea oceanography', in N. S. Heaps (ed.), *Coastal and Estuarine Sciences*, No. 4, *Three-dimensional Coastal Ocean Models*, American Geophysical Union, Washington, DC, 1987, pp. 71–106.
20. A. M. Davies and J. N. Aldridge, 'A stable algorithm for bed friction in three-dimensional shallow sea modal models', *Int. j. numer. methods fluids*, **14**, 477–493 (1992).
21. A. M. Davies, 'On the accuracy of finite difference and modal methods for computing tidal and wind wave current profiles', *Int. j. numer. methods fluids*, **12**, 101–124 (1991).
22. A. M. Davies, 'On using turbulence energy models to develop spectral viscosity models', *Continental Shelf Res.*, **11**, 1313–1353 (1991).
23. N. S. Heaps, 'Three-dimensional model for tides and surges with vertical eddy viscosity prescribed in two layers—I. Mathematical formulation', *Geophys. J. R. Astronom. Soc.*, **64**, 291–302 (1981).
24. A. M. Davies, 'On the importance of time varying eddy viscosity in generating higher tidal harmonics', *J. Geophys. Res.*, **95**, 20,287–20,312 (1990).
25. A. M. Davies and A. Owen, 'Three-dimensional numerical sea model using the Galerkin method with a polynomial basis set', *Appl. Math. Modell.*, **3**, 421–428 (1979).
26. N. S. Heaps and J. E. Jones, 'Development of a three-layered spectral model for the motion of a stratified sea. II. Experiments with a rectangular basin representing the Celtic Sea', in B. Johns (ed.), *Elsevier Oceanography Series*, Vol. 35, *Physical Oceanography of Coastal and Shelf Seas*, Elsevier, Amsterdam, 1983, pp. 401–465.